Advanced Intelligent Discovery

RESEARCH ARTICLE OPEN ACCESS

In Situ Contact Angle Measurement for Autonomous Spin Coating in Self-Driving Labs

Sven Fischer[1,2] | Micha Hiegle[1,2] | Holger Röhm[1,2]

[1]Karlsruhe Institute of Technology (KIT), Material Research Center for Energy Systems, Karlsruhe, Germany | [2]Karlsruhe Institute of Technology (KIT), Light Technology Institute, Karlsruhe, Germany

Correspondence: Holger Röhm (holger.roehm@kit.edu)

Received: 14 March 2026 | **Revised:** 6 May 2026 | **Accepted:** 28 May 2026

Keywords: computer vision | contact angle measurement | laboratory automation | self-driving laboratory | semantic segmentation | spin coating | thin-film photovoltaics

ABSTRACT

Current experimental workflows in solution-processed thin-film photovoltaics research are restricted to known solution combinations where solvent properties are predictable. To experimentally investigate the vast parameter space of new compounds, we must explore unknown material combinations using automated systems. However, this increases the risk of coating failures that previously required human judgment to detect. Integrating real-time process monitoring into existing deposition equipment is essential to close that gap. We present a vision-based add-on to commercial spin coaters that provides the process feedback missing from standard equipment—wetting assessment and substrate orientation for robotic retrieval—enabling fully automated coating workflows. Our hybrid software pipeline combines semantic segmentation using a width-scaled U-Net with classical geometric analysis, enabling simultaneous contact angle measurement and substrate pose estimation from a single RGB camera. We validated the module through an 11 h fully automated experiment, tracking hydrophobic recovery on plasma-treated substrates. By replacing human process supervision with machine vision, this system is a prerequisite for materials discovery in previously unexplored chemical regimes and transforms standard commercial spin coaters into components of Self-Driving Labs.

1 | Introduction

Computational screening has identified millions of promising material candidates for photovoltaics across organic semiconductors, perovskites, and metal oxides. The Harvard Clean Energy Project identified 2.3 million simulated compounds for organic photovoltaics [1], while 90 000 perovskites remain computationally predicted but untested. Only 3225 organic polymers are synthesized and 400 distinct perovskite composites are used in the Perovskite Database [2, 3]. This stark disparity between simulated and experimentally validated materials represents a fundamental bottleneck in photovoltaics research, necessitating automated Self-Driving Labs (SDLs).

Recent years have seen rapid progress in autonomous platforms for solution-processed thin-film research. The Ada platform demonstrated autonomous optimization of spin-coated hole-transport layers for perovskite solar cells [4], the SPINBOT system extended this to machine-learning-guided optimization of perovskite processing parameters [5] and the AMANDA platform was employed for fully autonomous device fabrication [6]. All these platforms share a common goal: discovering new materials that can be solution-processed, particularly via spin coating. These approaches to the experimental exploration of unknown chemical spaces and solvent combinations require real-time information on wetting behavior, which is currently not available in commercial spin coating equipment.

Sven Fischer and Micha Hiegle contributed equally to this study.

https://doi.org/10.1002/aidi.70139

Although there are various other viable deposition techniques such as blade coating, slot die coating and inkjet printing, spin coating remains the dominant lab-scale deposition method: Our analysis of an open-access perovskite database revealed that 97% of documented perovskite solar cells were manufactured with at least one spin-coated layer [7]. Spin coating enables rapid single-substrate processing of multilayer device architectures, making it ideal for material screening and small-area cells that minimize material consumption and fabrication defects. Limitations include poor scalability, material waste during spinning and, as with all solution-based methods, the requirement for orthogonal solvent systems between successive layers. However, this flexibility means new formulations may fail due to incompatibilities in viscosity, solubility, or wetting behavior on the substrate. Recent advances demonstrate that transmission spectra monitoring [8] or photoluminescence measurement [9] can provide real-time process feedback for adaptive automation during spin coating. However, these measurements are focused on optoelectronic properties that emerge during the drying of a wet film and do not directly monitor wetting properties that impact the film formation.

Automating spin coating requires solving two distinct problems: First, the system must determine whether a dispensed formulation is wetting the substrate successfully, enabling adaptive responses to coating failures in unexplored solvent spaces. Conventionally, this is achieved by measuring the wetting properties in an external setup prior to spin coating. Recent ML-based approaches have improved the accuracy and robustness of such goniometers [10]. At the platform level, RAISE has recently integrated automated contact angle measurement into a self-driving laboratory for interfacial formulation discovery [11], though it operates as a dedicated ex situ station. This ex situ approach is incompatible with high-throughput workflows where substrates must move efficiently through automated systems. Second, the robotic system that handles the sample must know the substrate's final orientation after spinning to execute precise retrieval. Standard spin coaters only accept speed, acceleration, and duration commands without feedback on these critical parameters. While angular sensors offer one solution, they require recessed chucks that impact airflow disturbance [12, 13], can cause capillary contamination [14] and require specific substrate sizes.

The measurement of a liquid's contact angle with a substrate, which is defined as the angle at the three-phase solid–liquid-vapor interface [15] can provide direct process feedback on the wetting of a liquid with unknown properties. According to ASTM D7334 standards, contact angles <45° indicate favorable wetting, with <20° denoting excellent conditions ([16]). Reduced contact angles correlate with improved film uniformity and fewer defects [17–19]. However, real surfaces exhibit contact angle hysteresis—a difference between the advancing angle (measured during liquid addition) and receding angle (measured during liquid removal) [20]. This hysteresis arises from surface roughness [21], chemical heterogeneity [22], and defects. Static contact angle measurements capture only a single state within this hysteresis range but are widely used for their simplicity and rapid measurement speed. Unlike ex situ measurement systems that employ a homogeneous background and controlled backlighting for high-contrast droplet contours, an in situ spin coater setup would present a challenging optical environment: variable substrate transparency, colored liquids, ejected droplets that contaminate the optics, and restricted positioning constraints. The classic approach for detection of the droplet outline is using edge detection algorithms [23], though recent advances employ neural networks for improved accuracy [10].

In this work, we address both spin coater automation challenges of wetting monitoring and sample position tracking in a single vision-based monitoring system integrated into a commercial spin coater, which transforms the system into a module for autonomous material screening. Our contributions are threefold: First, we demonstrate contact angle measurement via semantic segmentation under challenging optical conditions using a width-scaled U-Net architecture, eliminating dedicated goniometer requirements while achieving 4.15° agreement with commercial instruments. Second, we implement substrate orientation detection based on the semantic segmentation masks, achieving 0.8° σ through analysis-by-synthesis (AbS), ensuring safe robotic handling with 100% of measurements within $\pm 4.8°$ (6σ) tolerance. Third, we validate continuous automated operation through an 11 h experiment tracking hydrophobic recovery on plasma-treated substrates. By replacing human process supervision with machine vision, this add-on can be integrated into SDL's, enabling solar cell material discovery in previously unexplored chemical regimes and transforms standard spin coaters into SDL components.

2 | Methods

2.1 | Automated Spin Coater Setup

To realize a vision-based monitoring system, we combined a commercial spin coater (SUSS LabSpin 6) with a CCD camera (Basler ace acA3088-16). In order to achieve sufficient illumination for the image acquisition inside the spin coater we integrated a 3D-printed splash guard containing an LED strip (COB-LED, 93 CRI and 1200 lm/m). The schematic setup of the system is depicted in Figure 1.

We also provide a detailed technical drawing of the optical geometry, including the viewing inclination and the projected substrate dimensions on the sensor plane, in Figures S1–S3 of the

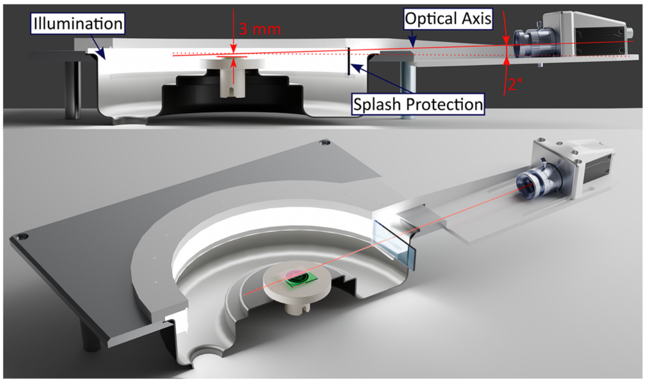

FIGURE 1 | Schematic image of a regular spin coater with a camera add-on. The optical axis is 3 mm above the spin coater center and inclined by 2°. The add-on has an LED strip for illumination and a replacable glass window to protect the camera.

Supporting Information. The full 3D model of the add-on, including a parametric drawing for adapting the field of view and mounting distance to different cameras, is publicly available via Onshape (link in the Data Availability Statement).

This setup only requires a line of sight of the camera at a low angle and could be adjusted to many common spin coater types. For contact angle measurements, a robotic handler places a substrate inside the spin coater, followed by a robotic pipette placing a droplet of the liquid on the substrate, and finally, a camera image is acquired that is used for further analysis.

2.2 | Hybrid Pipeline Architecture

To resolve the conflict between the stochastic nature of visual noise in the spin coater and the requirement for deterministic metrology, we developed a hybrid software architecture. Standard end-to-end deep learning approaches that directly convert an image to an output value act as "black boxes", lacking analytical correlation between geometric properties of objects and the output, while classical edge detection (Canny/Sobel) fails amidst the specular reflections and background contamination that is typical for spin coating.

Our solution is a two-stage hybrid pipeline that leverages the semantic robustness of deep learning for scene understanding and the precision of classical computer vision for quantification (Figure 2).

The first stage of the hybrid pipeline is semantic segmentation of the acquired image. The input RGB stream is processed by a lightweight U-Net inspired architecture [24]. Rather than regressing values directly, the network functions as an intelligent filter, classifying pixels into semantic layers: Droplet, Substrate, Pipette Tip (not shown), and Background. This effectively creates a "clean", noise-free binary representation of the physical state, masking out splashes, reflections, and variable lighting conditions that confound classical algorithms.

The second stage of the hybrid pipeline is the analysis. The segmented masks serve as the input for two parallel analytical branches. For wettability measurements, the droplet mask undergoes geometric fitting (ellipse/polynomial) to derive the contact angle, utilizing the entire contour to minimize local noise. The second branch determines the substrate rotation by comparing the substrate mask against a digital twin using an AbS loop that resolves the 6D pose (three dimensions of translation, three rotational axes).

A critical advantage of this topology is computational synergy. A single forward pass of the neural network extracts features for multiple distinct objectives simultaneously. The same inference cycle that determines wettability (via the droplet mask) also ensures robotic safety (via the substrate mask) and validates process integrity (via pipette tip detection). This shared computational burden enables the system to operate with low latency on standard workstation hardware, a prerequisite for real-time intervention in SDL workflows.

2.3 | Segmentation

The first stage of the vision pipeline utilizes our custom implementation of a convolutional neural network, referred to as UNetS. This architecture is derived from the U-Net topology [24], which was selected for its established efficiency in data-limited regimes [25]. To optimize the model for high-frequency in situ monitoring, we implemented a width-scaled variant that reduces the initial feature channels from 64 to 32. This modification reduces the model complexity to 7.8 million parameters, improving inference latency by a factor of 2.7 compared to the standard U-Net while maintaining high segmentation accuracy (Dice = 0.75).

To ensure generalization across varying laboratory conditions, a primary dataset of 406 images was aggregated from seven distinct experimental campaigns. The dataset covers varying substrate sizes, lighting environments, and diverse material combinations with contact angles ranging from 4° to 118° (see Figures S4 and S5). It was randomly partitioned into a training set ($N = 365$) and a validation set ($N = 41$). To evaluate the final model performance on unseen data without bias, an additional, independent test set ($N = 50$) was collected separately and not subjected to the random partitioning. Ground truth masks for droplets, substrates, and pipette tips were annotated manually with the Computer Vision Annotation Tool (CVAT). To combat overfitting and mimic the harsh optical environment of a spin coater, we applied an aggressive online data augmentation pipeline. This included photometric distortions (random color jittering, and grayscale conversion) to simulate changing LED intensities and optical

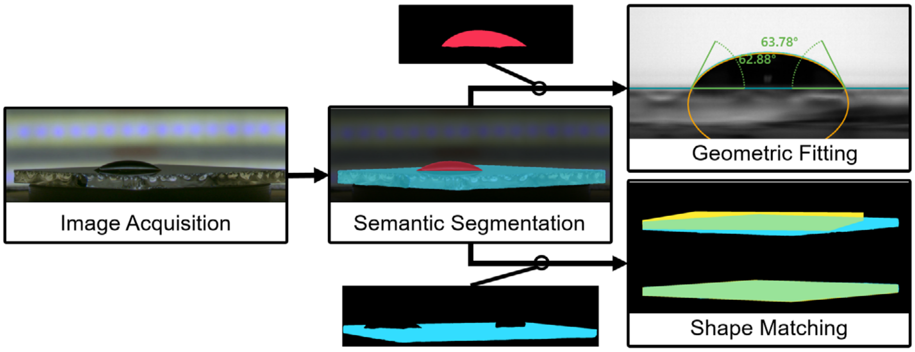

FIGURE 2 | Overview of the hybrid vision pipeline. The input image is processed by semantic segmentation, producing masks that feed two parallel branches: geometric fitting for contact angle measurement and shape matching for substrate pose estimation.

liquid properties and geometric transformations (perspective warps) to account for slight camera misalignments.

The model was trained using a composite “Combo Loss” function. It combines weighted cross-entropy with Soft Dice Loss to address the extreme class imbalance of the dataset, where the “Droplet” and “Pipette” classes occupy merely 0.9% and 0.4% of the pixel area, respectively, compared to “Substrate” (11.3%) and “Background” (87.4%). Finally, logical postprocessing using connected component analysis (CCA) filters artifacts smaller than 20 pixels (0.1 mm^2), ensuring only physically significant features are passed to the analytical modules.

2.4 | Contact Angle Measurement

The binary masks generated by the segmentation model provide a noise-free input for the contact angle measurement (Figure 3). The system first identifies the tri-phase contact points by detecting the maximum horizontal span of the droplet contour at the substrate interface, operating under the assumption of hydrophilic regimes ($\theta \leq 90°$), typical for thin-film spin coating. For hydrophobic cases ($\theta > 90°$), this assumption would detect a false elevated baseline, yielding an incorrect measurement below 90°.

For angle estimation, we evaluated both local (tangent/polynomial) and global (ellipse) fitting strategies. Since our preliminary analysis revealed that local tangent methods were highly sensitive to pixel-level noise around the tri-phase contact points, resulting in high measurement variance, we chose to implement global ellipse fitting. By minimizing the least-squares error over the entire droplet contour, this method effectively averages out local edge roughness, significantly improving measurement stability.

The contact angle is derived analytically from the tangent of the fitted ellipse at the tri-phase points. To ensure autonomous reliability, the system evaluates the validity of the fit by calculating the discriminant of the intersection between the ellipse equation and the substrate baseline (defined by the tri-phase points). If the discriminant is negative, indicating no real intersection, the ellipse is rejected as nonphysical. In such cases, the system automatically defaults to a parabolic fit, which provides numerical stability for flat droplets. Additional heuristic criteria, such as rejecting fits with aspect ratios exceeding 10 or excessive lateral displacement, further guarantee geometric plausibility before the final angle is extracted from the derivative of the fitted curve.

2.5 | Substrate Orientation Detection

The substrate orientation is determined using an AbS approach (Figure 4). Unlike direct regression methods that predict parameters from an image, this system operates as a feedback loop that iteratively refines a “digital twin” until it matches the observation.

The process begins with the “semantic segmentation” module, which feeds a clean binary mask of the physical substrate into the optimization loop. Inside this loop, the workflow cycles between two primary components. First, the “substrate and camera simulation” module acts as the forward model. It projects a sparse 3D representation of the substrate (defined by its eight corner vertices) onto the 2D image plane. This projection is then rasterized into a binary mask, serving as the hypothesis for the optimization loop. Second, in the “mask comparison and optimization” step, the system evaluates the discrepancy between this synthetic hypothesis and the real semantic mask, using a hybrid cost function L_{comb} which combines a region-based metric (dice similarity coefficient [DSC]) with a boundary-based metric (average surface distance [ASD]; detailed in Supporting Information Note S1)

$$L_{\text{comb}}(\alpha, \beta) = \alpha \cdot (1 - \text{DSC}) + \beta \cdot \frac{\text{ASD}}{d_{\text{norm}}}$$

This combination ensures robust gradient descent even when the shapes are partially disjoint while maintaining sensitivity to fine angular misalignments. Based on this metric, the optimizer adjusts the pose parameters and feeds them back into the simulation, closing the loop. This cycle repeats until the error is minimized, at which point the final optimized angle is output as part of the substrate position.

The core operational variable for safe robotic retrieval is the substrate’s in-plane rotation around the vertical z-axis (θ_z). Substrates used in thin-film research are typically square, introducing a 4-fold rotational symmetry that results in identical visual appearances at 90° intervals. Consequently, the visual optimization operates within a constrained angular window bounded between $-45°$ and $+45°$. To translate this visual data into actionable commands, the absolute angle of the robotic gripper is mapped to this $\pm 45°$ interval to define a zero-reference, enabling the system to map the optimizer’s results back to the robot’s coordinate system. Furthermore, the periodic nature of this optimization landscape can create local minima at the $\pm 45°$ boundaries. To prevent the optimizer from converging into a metastable state during a boundary crossing, we implemented a "Boundary Jump" heuristic. If the initial optimization converges within $\pm 20°$ of the $\pm 45°$ wrap-around limits, the system triggers a secondary optimization constrained to the complementary angular sector. The solver evaluates the loss of both hypotheses and returns the global minimum, ensuring robust alignment within the 90° rotational symmetry required by the robotic gripper.

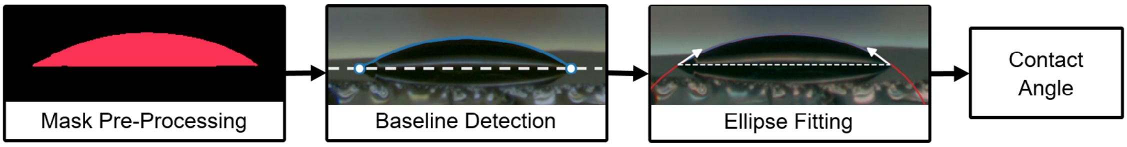

FIGURE 3 | Contact angle measurement pipeline. The segmented droplet mask undergoes baseline detection to identify the tri-phase contact points, followed by ellipse fitting to derive the contact angle.

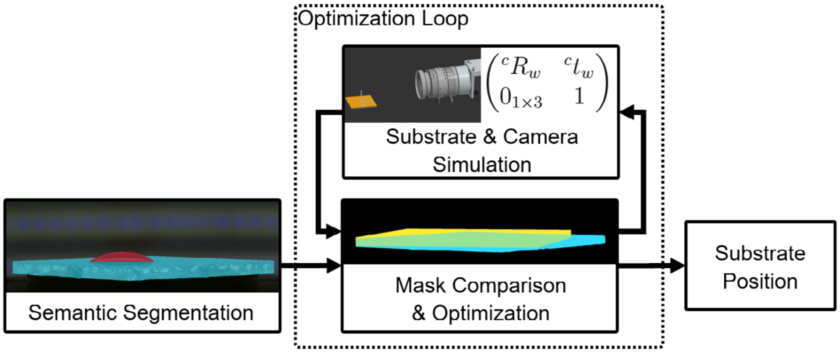

FIGURE 4 | AbS pose estimation. Substrate dimensions, camera parameters and the segmented mask are combined to optimize the projected digital twin against the real observation.

3 | Results and Discussion

We validated our system through four key experiments evaluating segmentation accuracy, orientation detection precision, contact angle measurement accuracy, and long-term autonomous operation capability.

3.1 | Segmentation Performance

To validate the architectural optimization of the segmentation model, the custom UNetS model was benchmarked against the standard U-Net topology. Inference latency was measured on a workstation equipped with an NVIDIA GeForce RTX 3060 Ti GPU. The benchmarking demonstrated that the model scaling strategy successfully decoupled inference speed from segmentation accuracy.

By reducing the initial feature channels, the parameter count was decreased by 75% (from 31.0 to 7.8 M). Crucially, this compression yielded an improvement in inference latency by a factor of 2.7, increasing throughput from 8.1 to 22.3 FPS on the test hardware. This acceleration is critical for capturing dynamic wetting events during the high-speed spin process.

Despite this reduction in capacity, the UNetS model maintained a Dice similarity score of 0.75 on the test dataset. While higher Dice scores are often pursued in pure segmentation tasks, this accuracy is functionally sufficient for the proposed hybrid pipeline. Since the segmentation mask serves primarily as a semantic noise filter, the subsequent global geometric fitting (Section 2.4) utilizes the overall droplet shape rather than pixel-level boundaries. This approach effectively compensates for minor segmentation roughness, ensuring robust contact angle extraction even in the presence of specular reflections, as illustrated in Figure 5. However, some existing systematic limitations can result in critical failure of the contact angle measurement. In particular, obstruction of the tri-phase point detection, such as when a satellite droplet merges with the primary segmentation mask, can lead to a faulty baseline (Figure 5a). During validation, this specific error mode was observed in <1% of cases. While currently handled via outlier rejection, future work could address this by expanding the training dataset to explicitly include adjacent satellite droplets.

3.2 | Contact Angle Accuracy

To verify the reliability of the in situ monitoring system, we conducted a two-tier validation strategy: first, isolating algorithmic precision through direct image reanalysis, and second, characterizing real-world performance through a cross-device comparison on physical substrates.

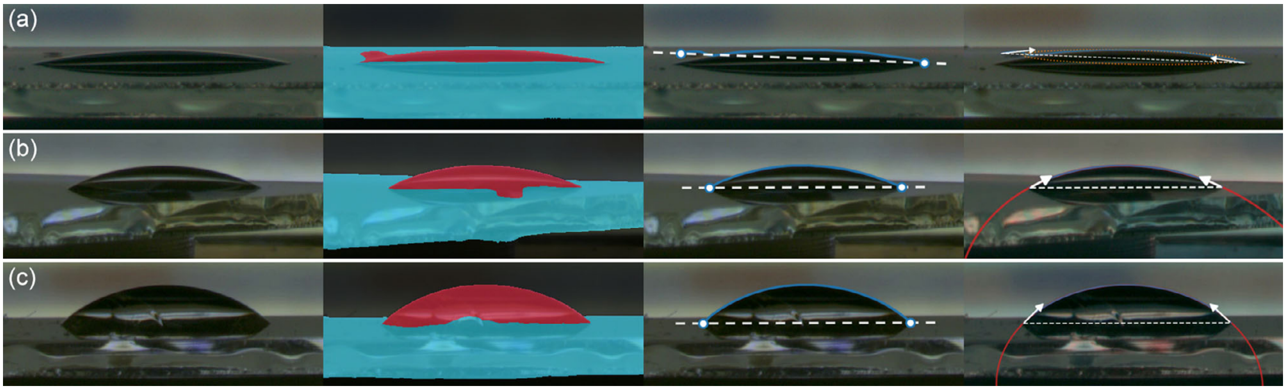

FIGURE 5 | Impact of segmentation artifacts on measurement accuracy. (a) Critical failure: A background artifact (satellite droplet) near the tri-phase point merges with the primary mask, distorting the baseline and causing a false contact angle result. (b,c) Robustness: Despite specular reflections at the droplet-substrate interface, the global geometric fitting successfully reconstructs the true contact angle.

3.2.1 | Algorithmic Precision and Software Validation

To quantify the measurement accuracy of our hybrid machine vision pipeline, we validated our approach against the commercially available dpiMAX analysis suite (OCA 25, DataPhysics Instruments) using a test dataset of 65 droplets captured within the spin coater environment (CA∈[4°, 90°]). Since the automated edge detection failed in the cluttered background of a spin bowl, the dpiMAX results were obtained via the manual contact angle fitting pipeline of the analysis suite to provide a baseline reference.

Figure 6 shows the comparison between this reference and our hybrid machine vision pipeline on identical image data, resulting in a Mean Absolute Error (MAE) of 2.05° ± 1.74°. The measurement data reveals a systematic bias of −1.58°, underestimating the true contact angle. We explore the root cause of this systematic underestimation and its potential for post-hoc calibration in Section 3.4. Nonetheless, this shows that the hybrid vision pipeline reconstructs the droplet profile with high fidelity, even in the presence of specular reflections and background contamination that prevented the dpiMAX software from automatic analysis.

3.2.2 | Experimental Performance and Surface Heterogeneity

Beyond algorithmic accuracy, we evaluated the complete measurement setup by comparing results with physical measurements on an OCA25 commercial goniometer. Ideally, both systems would measure the exact same droplet. However, mechanical disturbances during transport would shift the contact line and evaporation would alter the droplet geometry. Therefore, we utilized 23 standard glass substrates, dispensing fresh 10 μL droplets at spatially separated locations for each system (yielding 46 independent droplet measurements; see Supporting Information Note S2 for detailed protocol). The results of this cross-device study yielded an overall interdevice MAE of 4.15° (see Figure S6). Both devices achieved comparable intrasubstrate precision, with pooled standard deviations (σ) of 1.64° (OCA 25) and 2.23° (in situ system). These values align with the inherent baseline uncertainties of 0.5°–1° typical for sessile-drop goniometry [26].

The data reveal that the intersubstrate standard deviation ($\sigma = 4.08°$) substantially exceeded the intrasubstrate precision for both systems. This confirms that the primary source of measurement uncertainty is not the optical setup or the algorithm, but rather the physical surface heterogeneity (variations in local roughness and chemical state) inherent to prepared substrates [20]. For the intended application of materials acceleration, this level of accuracy is sufficient to reliably classify surface wettability against ASTM D7334 thresholds and detect process-critical wetting failures [16].

3.3 | Detection of Sample Orientation

With the trained segmentation model in place, we validated the pose estimation accuracy and robustness in two stages. In the first stage, square-shaped glass substrates (25 mm × 25 mm × 1 mm) where placed at 92 systematically stepped orientations on the training spin coater. In the second stage, the same model was deployed without retraining on a different spin coater with a different camera (Basler ace 2 a2A2048-114g5cBAS) and different lighting conditions, using 16 mm × 16 mm substrates across 200 placements. Due to the discrete rotational symmetry of the substrates, the orientation of the front-facing edge repeats every 90° and consequently, a range of $-44°$ to $+45°$ in 1° increments is sufficient to cover all unique orientations. We used the gripper angle of the robot that transfers the substrate into the spin coater as ground truth.

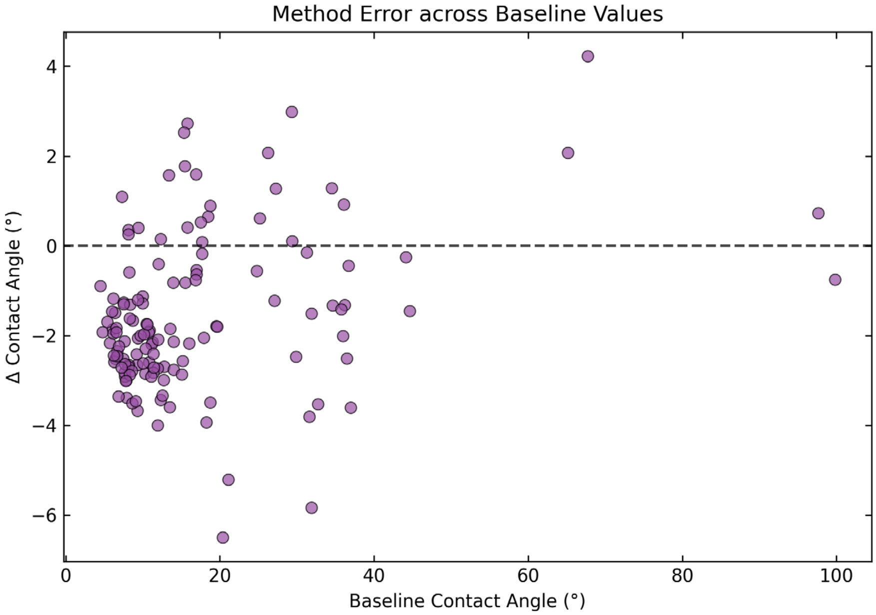

FIGURE 6 | Method error across baseline contact angle values. The error is defined as the contact angle calculated by the hybrid machine vision pipeline minus the manually fitted dpiMAX baseline. The scatter plot represents the analysis of 65 test droplets captured in situ within the spin coater environment, demonstrating consistent agreement across the measured range (4° to 99°) with an overall MAE of 2.05°.

For the 25 mm substrates, we evaluated all combinations of the loss weighting L_comb(α,β) on the training spin coater data and selected the best-performing configuration. The resulting optimal combined loss function $L_{\text{comb}}(30, 70)$ (30% DSC, 70% ASD) achieved a standard deviation of $\sigma = 0.8°$. Figure 7 shows the error as a function of ground truth angle for both substrate sizes. The system achieves a high accuracy for the 25 mm case with a standard deviation of 0.8°.

To assess suitability for automated handling, we evaluate the measurement precision against the 6σ tolerance criterion commonly applied in industrial process control [27, 28]. For the 25 mm substrates, the error distribution is consistent with a Gaussian (*Shapiro–Wilk* $p = 0.58$), with 71.7% within $\pm 1\sigma$, 98.9% within $\pm 3\sigma$, and 100% within $\pm 6\sigma$ (±4.8°), as shown in Figure 8 (left). For the 16 mm substrates on the second spin coater, the balanced weighting L_comb(50,50) yielded the best results ($\sigma = 2.3°$). The *Shapiro–Wilk* test rejects normality ($p = 0.0026$); as visible in Figures 7 (bottom) and 8 (right), the residual deviation reflects a systematic angle-dependent trend that we attribute to the AbS optimizer occasionally converging into shallow local minima when the available pixel information is reduced.

The resulting precision ensures reliable substrate retrieval by a robotic gripper, enabling safe handling without risk of collision or misalignment—a prerequisite for continuous autonomous operation.

The reduced precision on the 16 mm substrate has two origins: the available information in the signal is reduced due to optical effects, and the training data did not include the new surroundings. Due to the 2° field of view, the 25 mm substrate is projected to a height of only 0.13 mm. With the 16 mm substrate, this is further reduced to 0.08 mm, which decreases the available pixel area by 40%. The 25 mm substrate therefore provides 57 400 pixels in total, compared to 23 300 pixels for the 16 mm substrate. With fewer pixels available, the optimizer has less information to localize the substrate, increasing the angular uncertainty (Figure S6). Additionally, the segmentation operates fully out-of-distribution in camera hardware and optical environment simultaneously. Nonetheless, all measurements remain within the 6σ handling tolerance without any retraining, indicating that the training strategy generalizes meaningfully beyond its training conditions. This robustness toward changing conditions is highly desirable for SDL deployment.

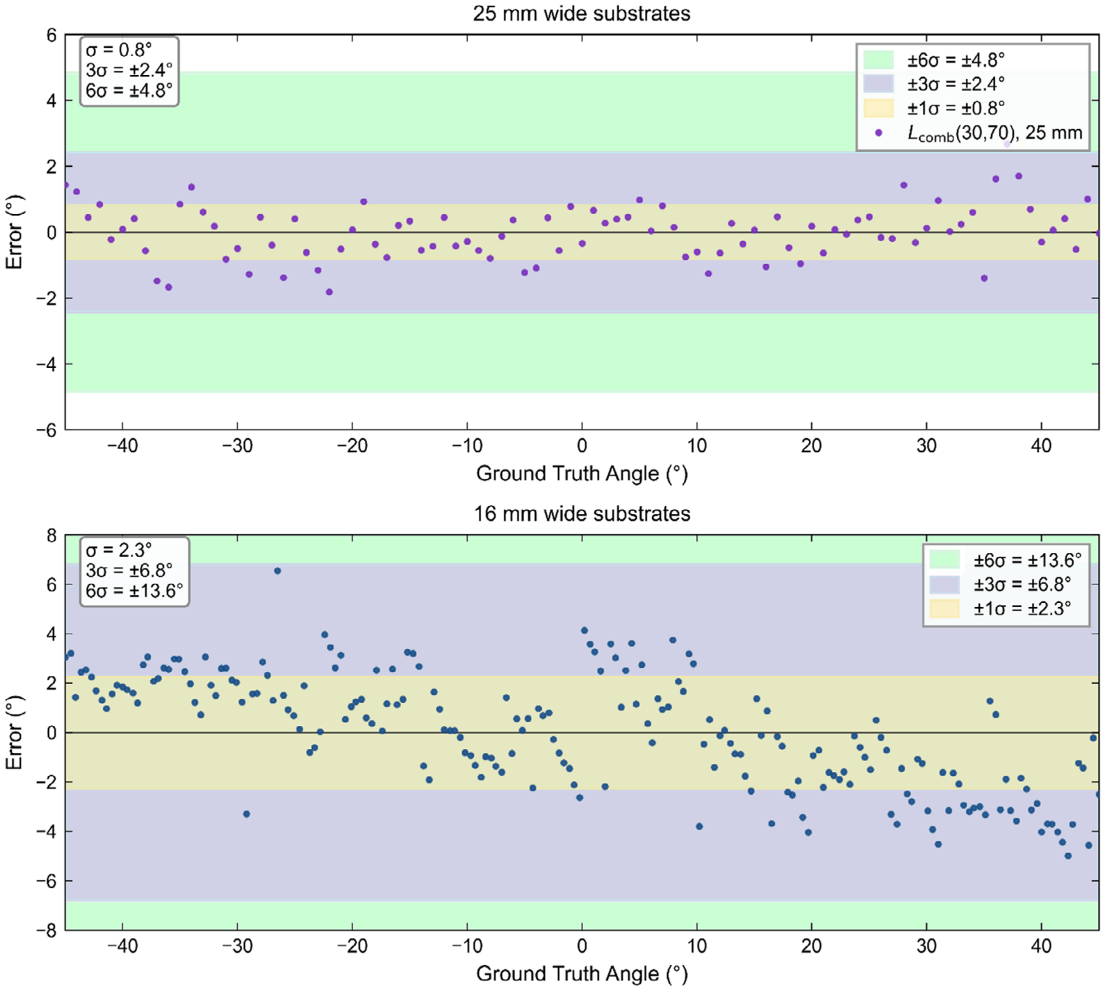

FIGURE 7 | Orientation detection error as a function of ground truth angle. Shaded bands indicate $\pm 1\sigma$, $\pm 3\sigma$, and $\pm 6\sigma$ tolerance zones. Top: 25 mm substrates on the training spin coater using L_comb(30,70) ($\sigma = 0.8°$). Bottom: 16 mm substrates deployed on a second spin coater with a different camera and lighting conditions using L_comb(50,50) ($\sigma = 2.3°$). While performance degrades, all measurements remain within an acceptable range for robotic substrate handling.

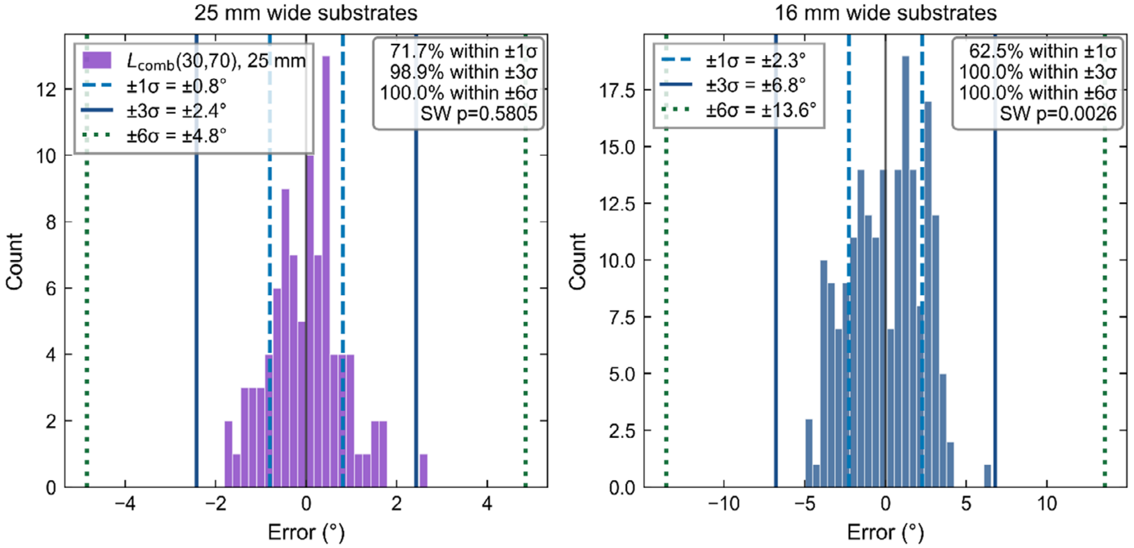

FIGURE 8 | Error distribution of orientation measurements for 25 mm wide (left) and 16 mm wide (right) substrates. For the 25 mm case, the distribution shows near-Gaussian behavior (Shapiro–Wilk $p = 0.58$), with 71.7% of measurements within ±1σ and 98.9% within ±3σ (±2.4°), and all measurements within the 6σ criterion (±4.8°). The 16 mm substrates, on a different setup than the one used for training, show a broader but still centered distribution ($\sigma = 2.3°$); the Shapiro–Wilk test rejects normality ($p = 0.0026$), which we attribute to the AbS optimizer occasionally converging into shallow local minima when pixel information is reduced.

To relate this precision to the actual handling requirement, we computed the process capability index $C_{pk} = T/(3\sigma)$, where T is the half-width of the angular tolerance set by the gripper geometry ($T_{25} = 9.9°$, $T_{16} = 34.0°$; see Figure S2). The resulting C_{pk} values of 4.1 (25 mm) and 4.0 (16 mm) exceed the $C_{pk} \geq 2.0$ threshold corresponding to Six Sigma process capability, confirming that the 6σ measurement spread occupies less than half of the available tolerance window.

3.4 | Automated Long-Duration Experiment

To validate its long-term reliability and integration of the vision-based monitoring system, we conducted an 11 h continuous experiment that involved automated contact angle measurements and the robotic handling based on the substrate orientation measurement: 35 glass substrates were cleaned following our aforementioned standard protocol, and then the substrate surfaces were activated via oxygen plasma-treatment. This surface activation via oxygen adsorption leads to a significantly reduced contact angle and hence, improved wetting of water, but the effect fades over time [29, 30]. The robotic gantry autonomously retrieved each substrate from a tray, transferred it to the spin coater, dispensed a 10 μL droplet of deionized water via a micropipette, and measured the contact angle at 20 min intervals—requiring no human intervention throughout the entire experiment. This also served as a simultaneous validation of the orientation detection, as the system successfully located and retrieved every substrate without failure.

We measured an initial contact angle of $\theta_{\text{init}} = 4.6°$ immediately after plasma activation. Over the 11 h observation window, the contact angle increased steadily to $\theta \approx 10.4°$, consistent with hydrophobic recovery driven by the readsorption of airborne hydrocarbons onto the activated glass surface [29, 30]. Figure 9a shows the resulting contact angles that were determined by the automated ellipse fitting and the comparison to results from the same images manually being reanalyzed via the DataPhysics OCA software (ground truth). A linear fit yielded recovery rates of 0.33 °/h (ground truth) and 0.39 °/h (automated system) indicating a minor multiplicative component of a systematic bias.

The low R^2 values (0.277 for ground truth, 0.347 for automated contact angle determination) do not indicate a weak trend but rather reflect the dominance of intersubstrate heterogeneity over the temporal signal. As established in Section 3.2, the intersubstrate standard deviation (σ = 4.08°–4.23°) substantially exceeds the intrasubstrate measurement precision (σ = 1.64°–2.23°). Since each substrate was measured only once—destructively, by dispensing a droplet—the scatter at any given time point is governed by this substrate-to-substrate variability, which is comparable to the total recovery range of 5.8° over 11 h. Hydrophobic recovery on inorganic surfaces generally follows logarithmic rather than linear kinetics [29, 31], with the fastest changes occurring within the first hours. Our 11 h experimental window likely captures the early, approximately linear portion of this longer-timescale process; at extended timescales, the contact angle would be expected to plateau as the surface approaches thermodynamic equilibrium.

Figure 9b shows the distribution of measurement errors between the automated and ground truth values, revealing a systematic bias of $-2.15° \pm 0.73°$. This underestimation likely arises from insufficient representation of low contact angles (<15°) in the segmentation training dataset, where the droplet profile becomes increasingly flat and difficult to segment. A post-hoc linear calibration ($\theta_{\text{calibrated}} = 0.947 \cdot \theta_{\text{ellipse}} + 2.29°$) reduced the MAE to 1.11° and would bring the two recovery rates into agreement; however, since this correction was derived from the same dataset, independent validation across a broader contact angle range is required before routine application.

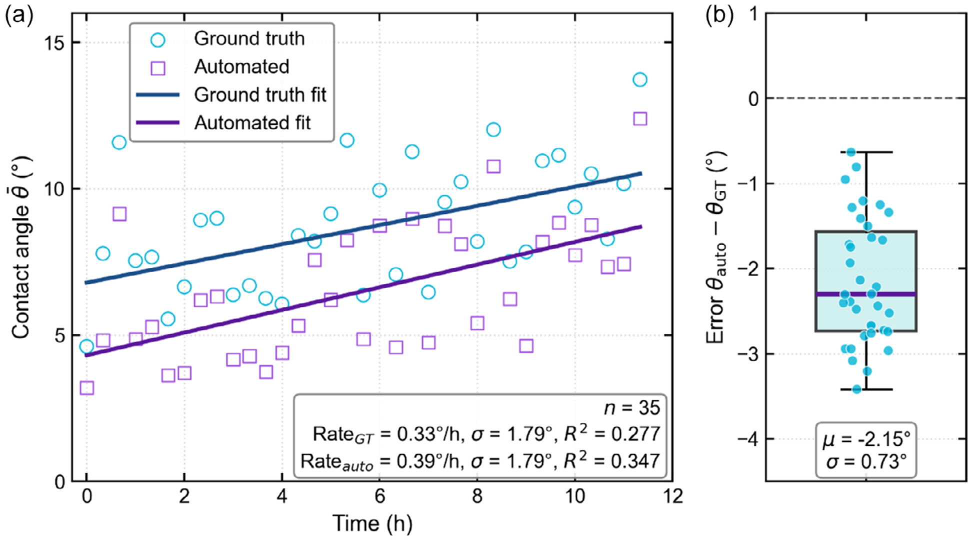

FIGURE 9 | Temporal evolution of water contact angle on plasma-treated glass substrates ($n = 35$). (a) Comparison between manual ground truth measurements and automated ellipse fitting showing systematic underestimation by the automated system. Linear fits yield recovery rates of 0.33 °/h (ground truth, $R^2 = 0.277$) and 0.39 °/h (automated, $R^2 = 0.347$). (b) Distribution of measurement errors revealing a mean bias of $-2.15^\circ \pm 0.73^\circ$.

Despite this uncorrected bias, the system reliably tracked the monotonic recovery trend over 11 h of fully automated operation. For process monitoring in an SDL context, the system's precision ($\sigma = 0.73^\circ$) is sufficient to resolve meaningful changes in wetting that can either stem from changes of the substrate surfaces, changed properties of the deposited liquids or both. This experiment confirms that the integrated vision pipeline can sustain continuous operation without drift or failure, a prerequisite for unsupervised material screening campaigns.

4 | Conclusion

Expanding materials discovery beyond established chemical spaces requires autonomous experimental systems capable of operating without human supervision. We present a vision-based monitoring system that integrates contact angle measurement and substrate pose estimation into a commercial spin coater, providing the sensory feedback necessary for autonomous operation in SDLs.

Our hybrid software architecture addresses the challenging optical environment of spin coating—variable substrate transparency, colored formulations, and contaminated optics—where conventional edge detection fails. By combining semantic segmentation using a width-scaled U-Net (UNetS) with classical geometric analysis, we achieved computational efficiency suitable for real-time monitoring while maintaining measurement accuracy. The UNetS architecture reduced model parameters by 75% (from 31.0 to 7.8 M), enabling inference at 22.3 FPS on standard GPU hardware while preserving segmentation performance (Dice = 0.75).

For contact angle measurements, our global ellipse fitting approach achieved 2.05° MAE compared to a commercial goniometer (OCA 25) when measuring water droplets on glass substrates. This accuracy is sufficient to classify surface wettability according to ASTM D7334 standards, enabling automated detection of coating failures due to poor wetting. The substrate pose estimation via AbS achieved 0.8° σ with 100% of measurements within the ±4.8° (6σ) tolerance required for safe robotic handling, ensuring reliable substrate retrieval without human intervention.

We validated continuous automated operation through an 11 h experiment tracking hydrophobic recovery on 35 plasma-treated glass substrates. The system successfully detected the monotonic increase in contact angle from 4.6° to 10.4° (recovery rate = 0.4°/h), demonstrating the capability to monitor subtle surface energy changes over extended periods without drift or failure. This experiment simultaneously validated both the contact angle measurement and pose estimation modules, with the robotic gantry autonomously retrieving all substrates at 20 min intervals without positioning errors.

4.1 | Current Limitations and Outlook

The present validation focused on water-on-glass systems to establish measurement accuracy against reference instrumentation. Future work must extend validation to formulations used in thin film research, for example, organic solvents (chlorobenzene, DMF, DMSO), lead halide perovskite precursors, polymer solutions and nanoparticle dispersion, to fully realize the system's potential for exploring unknown chemical spaces. The systematic underestimation of contact angles below 15° (bias of $-2.15^\circ \pm 0.73^\circ$ in the long-duration experiment) indicates insufficient representation of extreme wetting regimes in the training dataset. Expanding the dataset to include contact angles from 0° to 90° would improve accuracy across the full wettability spectrum. Since the demonstrated system identifies the tri-phase contact points for contact angle fitting by detecting the maximum horizontal span of the droplet contour, contact angle determination is not reliable for angles >90°.

The modular architecture of our hybrid pipeline enables transfer to other deposition methods and experimental stations within Materials Acceleration Platforms. The same semantic segmentation framework could be adapted for blade coating monitoring or pick-and-place processes from flat surfaces. More fundamentally, by demonstrating that standard commercial spin coaters can be upgraded with autonomous capabilities through vision-based monitoring, we provide a pathway for existing laboratory equipment to participate in SDL workflows without requiring specialized hardware replacement.

This work contributes to the broader vision of autonomous materials discovery by replacing human process supervision with machine vision in one of the most widely used deposition techniques in thin film research. While the path from automated experimentation to accelerated materials discovery requires integration of multiple autonomous systems—synthesis robots, characterization modules, and optimization algorithms—each component must demonstrate reliable unsupervised operation. Our system establishes that vision-based monitoring can provide the necessary sensory feedback for autonomous spin coating, removing a key bottleneck in the experimental pipeline toward exploration of vast chemical spaces.

Acknowledgments

Sven Fischer and Holger Röhm acknowledge funding by the Carl-Zeiss Foundation under the project “KeraSolar”. Holger Röhm also acknowledges support by the Helmholtz Association (38.01.02) under the research program “Materials and Technologies for the Energy Transition” (MTET). The authors thank A. Colsmann for fruitful discussions and J. Bruder, S. Coen, R. Datta, S. Denk, and K. Fischer for contributing segmentation training data.

Sven Fischer acknowledges the use of the large language model Claude (Anthropic), and Micha Hiegle acknowledges the use of Gemini (Google) for assistance with manuscript preparation, including language editing, text revision, structural feedback, and coding support during software development. All scientific content, experimental design, data collection, analysis, and interpretation were performed solely by the authors, who take full responsibility for the accuracy and integrity of the work.

Open Access funding enabled and organized by Projekt DEAL.

Funding

This study was supported by Helmholtz Association (MTET 38.01.02); Carl-Zeiss-Stiftung (KeraSolar).

Conflicts of Interest

The authors declare no conflicts of interest.

Data Availability Statement

Additional data that support the findings of this study are provided in the Supporting Information. Code examples for the computer vision system are openly available at https://gitlab.kit.edu/sven.fischer/spincoater_monitoring.

The 3D model of the camera add-on, including STEP files and a parametric Onshape drawing for adapting the optical setup to different cameras and spin coaters, is available in the same repository and via Onshape at: https://cad.onshape.com/documents/942fed0653b247265ef0ad7e/w/a0ded3e744f7ec5f7834da02/e/6e97a5fd8d50eef7385ac1ae?renderMode=0&uiState=69f209187fe03d7472b5767b.

References

1. J. Hachmann, R. Olivares-Amaya, A. Jinich, et al., “Lead Candidates for High-Performance Organic Photovoltaics from High-Throughput Quantum Chemistry – the Harvard Clean Energy Project,” *Energy & Environmental Science* 7, no. 2 (2014): 698–704, https://doi.org/10.1039/C3EE42756K.

2. X. Liu, X. Zhang, Y. Wu, X. Ju, C. Ye, and W. Zhang, “OPECM: A Comprehensive Dataset for Organic Polymer Energy Conversion Materials Enabling Data-Driven Interpretative Analysis,” *Physical Review Materials* 9, no. 12 (2025): 125405, https://doi.org/10.1103/tqfw-w29l.

3. E. Unger and T. J. Jacobsson, “The Perovskite Database Project: A Perspective on Collective Data Sharing,” *ACS Energy Letters* 7, no. 3 (2022): 1240–1245, https://doi.org/10.1021/acsenergylett.2c00330.

4. B. P. MacLeod, F. G. L. Parlane, T. D. Morrissey, et al., “Self-Driving Laboratory for Accelerated Discovery of Thin-Film Materials,” *Science Advances* 6, no. 20 (2020): eaaz8867, https://doi.org/10.1126/sciadv.aaz8867.

5. J. Zhang, B. Liu, Z. Liu, et al., “Optimizing Perovskite Thin-Film Parameter Spaces with Machine Learning-Guided Robotic Platform for High-Performance Perovskite Solar Cells,” *Advanced Energy Materials* 13, no. 48 (2023): 2302594, https://doi.org/10.1002/aenm.202302594.

6. J. Zhang, J. A. Hauch, and C. J. Brabec, “Toward Self-Driven Autonomous Material and Device Acceleration Platforms (AMADAP) for Emerging Photovoltaics Technologies,” *Accounts of Chemical Research* 57, no. 9 (2024): 1434–1445, https://doi.org/10.1021/acs.accounts.4c00095.

7. T. J. Jacobsson, A. Hultqvist, A. García-Fernández, et al., “An Open-Access Database and Analysis Tool for Perovskite Solar Cells Based on the FAIR Data Principles,” *Nature Energy* 7, no. 1 (2022): 107–115, https://doi.org/10.1038/s41560-021-00941-3.

8. T. Raab, T. Mayer, T. Seewald, and L. Schmidt-Mende, “Resolving the Spin Coating Process via In Situ Transmission Measurements,” *The Journal of Physical Chemistry C* 126, no. 45 (2022): 19542–19548, https://doi.org/10.1021/acs.jpcc.2c06337.

9. S. Biberger, M. Spies, K. Schötz, et al., “Reactive Spin Coating Based on Real-Time *In Situ* Feedback for Improved Control of Perovskite Thin Film Fabrication,” *Journal of Materials Chemistry C* 12, no. 18 (2024): 6415–6422, https://doi.org/10.1039/D3TC04361D.

10. H. Kabir and N. Garg, “Machine Learning Enabled Orthogonal Camera Goniometry for Accurate and Robust Contact Angle Measurements,” *Scientific Reports* 13, no. 1 (2023): 1497, https://doi.org/10.1038/s41598-023-28763-1.

11. M. Nazeri, S. Mei, J. Watchorn, et al., “RAISE: A Self-Driving Laboratory for Interfacial Property Formulation Discovery,” *Digital Discovery* 5 (2026): 2254–2270, https://doi.org/10.1039/D5DD00531K.

12. Q. Liu, Y. Yan, L. Meng, et al., “Influence of Airflow Disturbance on the Uniformity of Spin Coating Film Thickness on Large Area Rectangular Substrates,” *Coatings* 12, no. 9 (2022): 1253, https://doi.org/10.3390/coatings12091253.

13. G. A. Luurtsema, “Spin Coating for Rectangular Substrates (UCB/ERL M97/49),” 1997, http://www2.eecs.berkeley.edu/Pubs/TechRpts/1997/3265.html.

14. Q. Liu and P. Zhou, “Effect of Recessed Chuck Slits on the Edge Buildup in Spin Coating for Rectangular Substrates,” *Progress in Organic Coatings* 200 (2025): 108994, https://doi.org/10.1016/j.porgcoat.2024.108994.

15. T. Young, “III. An Essay on the Cohesion of Fluids,” *Philosophical Transactions of the Royal Society of London* 95 (1805): 65–87, https://doi.org/10.1098/RSTL.1805.0005.

16. D01 Committee, *Practice for Surface Wettability of Coatings, Substrates and Pigments by Advancing Contact Angle Measurement* (ASTM International, n.d.), https://doi.org/10.1520/D7334-08R22.

17. A. Al-Ashouri, M. Marčinskas, E. Kasparavičius, et al., “Wettability Improvement of a Carbazole-Based Hole-Selective Monolayer for Reproducible Perovskite Solar Cells,” *ACS Energy Letters* 8, no. 2 (2023): 898–900, https://doi.org/10.1021/acsenergylett.2c02629.

18. Y. Ma, C. Liu, M. Zhang, and Y. Mai, “Review on the Effects of Solvent Physical Properties on the Performance of Slot-Die Coated Perovskite Solar Cells,” *Surface Science and Technology* 2, no. 1 (2024): 25, https://doi.org/10.1007/s44251-024-00054-5.

19. X. Yan, M. Yang, W. Li, et al., “Optimizing Buried Interface Quality in Inverted Perovskite Solar Cells by Modulating the Spatial Orientation of Polymer Hole Transport Materials Using Rigid Copolymer Units,” *Dyes and Pigments* 236 (2025): 112676, https://doi.org/10.1016/j.dyepig.2025.112676.

20. T. Huhtamäki, X. Tian, J. T. Korhonen, and R. H. A. Ras, “Surface-Wetting Characterization Using Contact-Angle Measurements,” *Nature Protocols* 13 (2018): 1521–1538, https://doi.org/10.1038/S41596-018-0003-Z.

21. R. N. Wenzel, “Resistance of Solid Surfaces to Wetting by Water,” Industrial and Engineering Chemistry 28 (1936): 988–994, https://doi.org/10.1021/IE50320A024.

22. A. B. D. Cassie and S. Baxter, “Wettability of Porous Surfaces,” 1944, https://doi.org/10.1039/TF9444000546.

23. R. Akbari and C. Antonini, “Contact Angle Measurements: From Existing Methods to an Open-Source Tool,” *Advances in Colloid and Interface Science* 294 (2021): 102470, https://doi.org/10.1016/j.cis.2021.102470.

24. O. Ronneberger, P. Fischer, and T. Brox, “U-Net: Convolutional Networks for Biomedical Image Segmentation,” (arXiv: 1505.04597). arXiv (2015), https://doi.org/10.48550/arXiv.1505.04597.

25. M. Solopov, E. Chechekhina, A. Kavelina, et al., “Comparative Study of Deep Transfer Learning Models for Semantic Segmentation of Human Mesenchymal Stem Cell Micrographs,” *International Journal of Molecular Sciences* 26, no. 5 (2025): 2338, https://doi.org/10.3390/ijms26052338.

26. M. Vuckovac, M. Latikka, K. Liu, T. Huhtamäki, and R. H. A. Ras, “Uncertainties in Contact Angle Goniometry,” *Soft Matter* 15, no. 35 (2019): 7089–7096, https://doi.org/10.1039/C9SM01221D.

27. D. C. Montgomery, *Introduction to Statistical Quality Control*, 5. ed., internat ed. (Wiley, 2005).

28. A. Schulze and E. Dietrich, “Statistische Verfahren zur Maschinen- und Prozessqualifikation (6., vollst. überarb. Aufl., [elektronische Ressource]),” Hanser, 2009, https://doi.org/10.3139/9783446420847.

29. V. Jokinen, P. Suvanto, and S. Franssila, “Oxygen and Nitrogen Plasma Hydrophilization and Hydrophobic Recovery of Polymers,” *Biomicrofluidics* 6, no. 1 (2012): 016501-016501-016510.https://doi.org/10.1063/1.3673251.

30. P. Verding, R. Mary Joy, D. Reenaers, et al., “The Influence of UV–Ozone, O2 Plasma, and CF4 Plasma Treatment on the Droplet-Based Deposition of Diamond Nanoparticles,” *ACS Applied Materials & Interfaces* 16, no. 1 (2024): 1719–1726, https://doi.org/10.1021/acsami.3c14014.

31. G. Primc and M. Mozetič, “Hydrophobic Recovery of Plasma-Hydrophilized Polyethylene Terephthalate Polymers,” *Polymers* 14, no. 12 (2022): 2496, https://doi.org/10.3390/polym14122496.

Supporting Information

Additional supporting information can be found online in the Supporting Information section.